AFRL-AFOSR-UK-TR-2022-0011

Theoretical studies of fundamental processes relevant to diode pumped alkali lasers

Rosenwaks, Salman
BEN GURION UNIVERSITY OF THE NEGEV
1 BEN-GURION BLVD.
BEER SHEVA, , 84105
IL

12/09/2021
Final Technical Report

Air Force Research Laboratory
Air Force Office of Scientific Research
European Office of Aerospace Research and Development
Unit 4515 Box 14, APO AE 09421

REPORT DOCUMENTATION PAGE

Form Approved
OMB No. 0704-0188

1. REPORT DATE *(DD-MM-YYYY)*	**2. REPORT TYPE**	**3. DATES COVERED** *(From - To)*
09-12-2021	Final	15 Jun 2018 - 14 Jun 2021

4. TITLE AND SUBTITLE
Theoretical studies of fundamental processes relevant to diode pumped alkali lasers

5a. CONTRACT NUMBER

5b. GRANT NUMBER
FA9550-18-1-0204

5c. PROGRAM ELEMENT NUMBER
61102F

6. AUTHOR(S)
Salman Rosenwaks

5d. PROJECT NUMBER

5e. TASK NUMBER

5f. WORK UNIT NUMBER

7. PERFORMING ORGANIZATION NAME(S) AND ADDRESS(ES)
BEN GURION UNIVERSITY OF THE NEGEV
1 BEN-GURION BLVD.
BEER SHEVA, 84105
IL

8. PERFORMING ORGANIZATION REPORT NUMBER

9. SPONSORING/MONITORING AGENCY NAME(S) AND ADDRESS(ES)
EOARD
UNIT 4515
APO AE 09421-4515

10. SPONSOR/MONITOR'S ACRONYM(S)
AFRL/AFOSR IOE

11. SPONSOR/MONITOR'S REPORT NUMBER(S)
AFRL-AFOSR-UK-TR-2022-0011

12. DISTRIBUTION/AVAILABILITY STATEMENT
A Distribution Unlimited: PB Public Release

13. SUPPLEMENTARY NOTES

14. ABSTRACT
Theoretical studies of basic kinetic and optical processes relevant to DPALs that strongly affect the operation of these lasers and governing their output power and efficiency as well as studies of the output beam quality have been performed. The results were compared with experimental results obtained in our and other labs. Our main activity in the reported period concentrated on the following subjects: i) Dependence of static K DPAL performance on addition of methane: 3D CFD modeling and comparison with experimental results. ii) Velocity dependence of the performance of flowing-gas K DPAL with He and He/CH4 buffer gases: 3D CFD modeling and comparison with experimental results. iii) 3D CFD modeling of flowing-gas Rb DPALs: effects of buffer gas composition and of ionization of high lying Rb states. iv) Quantum mechanical computations of the dissociative recombination rate constant of K_2^+ ions in the gain medium of K DPAL: calculations of the potential energy surfaces for highly excited dissociative states of the ground state of the molecular ion and their crossing points. v) Calculations of the quenching cross-section of the excited electronic levels of Rb by methane using quantum mechanics methods. vi) Detailed theoretical study of controlling the beam quality in DPALs by changing the resonator parameters.

15. SUBJECT TERMS

16. SECURITY CLASSIFICATION OF:			**17. LIMITATION OF ABSTRACT**	**18. NUMBER OF PAGES**	**19a. NAME OF RESPONSIBLE PERSON**
a. REPORT	**b. ABSTRACT**	**c. THIS PAGE**			NATHANIEL LOCKWOOD
U	U	U	SAR	37	**19b. TELEPHONE NUMBER** *(Include area code)* 314-235-6005

Grant Number **FA9550-18-1-0204**

Research title:

Theoretical Studies of Fundamental Processes Relevant to Diode Pumped Alkali Lasers

Final Performance Report for the Period 15.6.18 – 31.12.21

Principal Investigators:
Prof. Boris Barmashenko and Prof. Zamik Rosenwaks
Department of Physics
Ben-Gurion University of the Negev

Table of Contents Page

I. Summary

Theoretical studies of basic kinetic and optical processes relevant to DPALs that strongly affect the operation of these lasers and governing their output power and efficiency as well as studies of the output beam quality have been performed. The results were compared with experimental results obtained in our and other labs. Our main activity in the reported period concentrated on the following subjects:

i) Dependence of static K DPAL performance on addition of methane: 3D CFD modeling and comparison with experimental results. The results are reported in Ref. 1.

ii) Velocity dependence of the performance of flowing-gas K DPAL with He and He/CH_4 buffer gases: 3D CFD modeling and comparison with experimental results. The results are reported in Ref. 2.

iii) 3D CFD modeling of flowing-gas Rb DPALs: effects of buffer gas composition and of ionization of high lying Rb states. The results are reported in Refs. 3 and 4.

iv) Quantum mechanical computations of the dissociative recombination rate constant of K_2^+ ions in the gain medium of K DPAL: calculations of the potential energy surfaces for highly excited dissociative states of K_2, the ground state of the molecular ion K_2^+ and their crossing points.

v) Calculations of the quenching cross-section of the excited electronic levels of Rb by methane using quantum mechanics methods.

vi) Detailed theoretical study of controlling the beam quality in DPALs by changing the resonator parameters. The results are reported in Refs. 5 and 6.

II. Introduction

Diode pumped alkali lasers (DPALs), operating at ~ 800 nm, are currently extensively studied due to their great potential as High Energy Lasers (HEL) which are major components in Laser Weapons Systems. In spite of the impressive operation features, different fundamental physical processes can limit the output power. These processes, schematically depicted in Fig. 1, include finite relaxation rate between the fine-structure levels $n^2P_{3/2}$ and $n^2P_{1/2}$, and quenching of these levels, photoexcitation and ionization of the alkali atoms, quenching of the high electronic levels of these atoms, heating of the gain medium and non-uniform spatial distribution of its temperature [7-9]. The heat

release due to relaxation between the fine-structure levels of alkali atoms and quenching of these levels results in considerable increase of the temperature in the lasing medium, which can achieve several hundred K. This temperature rise can result in decrease of the pump absorption. Moreover, photoexcitation of alkali atoms by pump and laser radiation and energy pooling collisions, followed by photo- and Penning-ionization of the excited atoms, may result in reduction of the density of neutral atoms participating in the lasing.

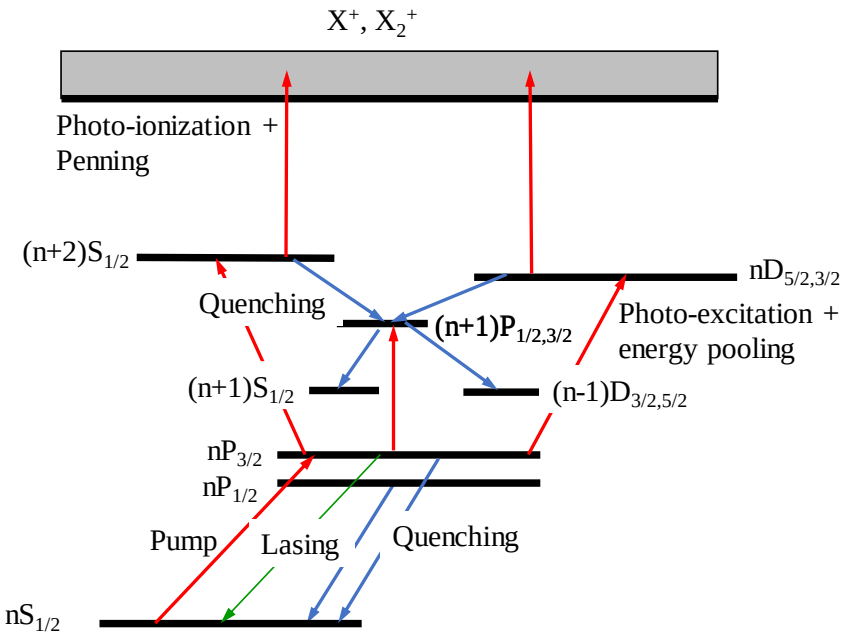

Fig. 1. Excitation, ionization and quenching processes in DPAL gain medium. X=Cs, Rb or K atoms.

All the aforementioned processes contribute to decrease of the efficiencies of DPALs and to degradation of their output lasing power and lasing termination. A fundamental study of all these processes, and in particular their influence on the operation of different DPALs, as well as the calculation of their rate constants is very important for the development of methods for scaling DPAL to output power of 100 kW and above.

Extensive research of DPALs [7-9] during the past decade examined the three alkali atoms Cs, Rb and K as potential candidates for development of a high power DPAL. All three DPALs have their positive and negative features, and each of them has been studied by various research groups. Recently, however, K DPAL has attracted special attention due to its unique kinetic and spectroscopic properties. This laser has very high quantum efficiency (99.6%) and can operate with low pressure (~1 atm) He buffer gas [7,10],

which eliminates the problem of chemical reaction of highly excited alkali atoms with hydrocarbons, limiting, in particular, the output power of Cs DPALs operating with hydrocarbon buffer. Noticeable results were reported for K flowing-gas laser, where output power of 3 kW was achieved and optical-to-optical efficiency reached 58% [11].

Until recently the general consensus was that K DPAL can work efficiently with hydrocarbon free He buffer gas since the energy mismatch between the $4^2P_{3/2}$ and $4^2P_{1/2}$ is only a 58 cm^{-1} and He can be an efficient relaxer of $4^2P_{3/2}$ [10]. However, recent experiments performed in Air Force Research Laboratory (AFRL) [12], US Air Force Academy (USAFA) [13,14] and Air Force Institute of Technology (AFIT) [15] showed that addition of a few percent of methane to He buffer gas results in substantial improvement of K DPAL operation.

In the present project the DPAL 3D computational fluid dynamics (CFD) model developed in our previous works [16,17] was used to study the effect of the buffer gas composition on the performance of static K DPAL. To explain the sharp increase in laser power with the addition of CH_4 to the He buffer gas, the model was supplemented with calculations of electron heating and the effect of high electron temperature on the ambipolar diffusion of K ions; our calculations showed that these processes are especially important for pure He and very small amounts of CH_4. In addition, the strong influence of the rate constants of ion-electron recombination on the laser power was analyzed.

The aforementioned processes are especially important for pure He buffer gas where high T_e results in fast ambipolar diffusion of K ions to the wall and depletion of the neutral K atoms in the lasing region. K atoms density can be restored by a gas flow that supplies the lasing region by fresh K atoms. As estimated in [13], for efficient operation of flowing-gas K DPAL with pure helium buffer gas, a considerable flow velocity of about 100 m/s should be applied. We performed an accurate 3D CFD modeling of the flowing-gas K DPAL taking into account the diffusion and ionization processes and found that the velocity required for the efficient laser operation is much higher than that estimated in [13] for both end and transverse pump geometries. The predictions of the model were compared with experimental results obtained at AFIT [15].

The laser power in K DPALs is strongly affected by ion-electron recombination, the rate of which is determined by the rate of dissociative recombination of K_2^+. Measured values of the rate constant of this process have not been published. For Cs the measured values of the dissociative recombination rate constant range from 52.6×10^{-14} [18] to

$1x10^{-14}$ m^3/s [19]. Therefore, it is very important to perform quantum mechanical computations of this rate. These computations require knowledge of the potential energy surfaces for highly excited dissociative states of K_2, the ground state of the molecular ion K_2^+ and their crossing points, which we calculated in this project.

Rb DPAL has certain advantages over the other two extensively studied DPALs using Cs and K atoms. The main advantage of Rb over Cs DPAL is the ability to work with pure He as buffer gas, while Cs laser works only when hydrocarbon-He mixtures are used as buffers [7]. At the same time, the optical efficiency and gain of the Rb laser are almost the same as those of the Cs laser [10,20]. The advantage of Rb over K DPAL is that the operation temperature in the former is lower and the energy mismatch between the fine structure *P* levels is larger than in the latter [7]. The fine structure *P* levels are usually in thermal equilibrium. Consequently, due to the larger Boltzmann exponent, the population inversion density and, hence, the gain in Rb DPAL is much higher, and the threshold pump power is much lower than in the K laser [10,20].

There is only scarce information on experiments with high power Rb lasers [12,21], but detailed theoretical studies are available. In a recent publication of Gavrielides *et al* [22], devoted to in-depth modeling of 100 kW class Rb laser, similar to the 30-kW device run by LLNL [21], it is shown that such a laser can operate with pure He buffer gas. Since the energy mismatch between the $5^2P_{3/2}$ and $5^2P_{1/2}$ levels of Rb is 238 cm^{-1}, high pressure of He, typically 15 atm, is needed in order to enhance the relaxation between them [22]. However, the Gavrielides model [22] is one-dimensional and uses a three-level kinetic scheme, ignoring the unresolved question of the possible ionization effect in Rb DPAL. Thus, it is of interest to apply more elaborate models for studying Rb DPALs.

We performed an accurate 3D CFD modeling of flowing-gas Rb DPAL with low (about several tens W) and high (about several tens kW) pump power. In contrast to the 1D three-level model [22], the present model, based on our model of the flowing-gas K DPAL [2], considers the processes of excitation of high levels of Rb, ionization, ion-electron recombination and heating of electrons affecting the diffusion coefficient of Rb ions. These processes are especially important for high-power lasers. For pure He buffer gas, the calculated results are compared with the results of [22] and it is found out how the above-mentioned processes affect the laser efficiency.

Fast quenching of the high electronic levels of Rb by the hydrocarbon molecules may decrease the density of the atoms in high electronic levels and retard the ionization and

chemical reactions rates. Calculations of the cross section for the quenching of excited electronic levels of Rb by methane using methods of quantum mechanics performed in this project are very important for understanding the operation of this laser.

Another important task is inclusion of optical aspects into the models of DPALs and in particular finding ways for substantial improvement of the output laser beam quality M^2 reducing it to close to unity. Using the optical model of multi-transverse mode operation we found that changing the length of the resonator, and/or the radius of curvature of the high reflection mirror, leaving all other parameters of the laser unchanged, makes it possible to control and improve the beam quality.

III. Methods, Assumptions and Procedures

ANSYS FLUENT 3D CFD code was used to solve the flow and the species conservation equations coupled to the molecular transport and beam propagation equations. The temperature distribution in the flowing medium was found using the energy conservation equation. The same 3D CFD code as that developed in [16,17] was employed. The gas dynamic equations were solved by a transient model, and the coupled kinetic rate equations for the populations of the electronically excited states of K or Rb atom were solved analytically at each time step, according to the perturbation theory introduced in [15]. However, the total density of neutral K or Rb atoms and the density of K_2^+ and Rb_2^+ ions were calculated using non-stationary transport equations taking into account the diffusion of neutral atoms from the cell wall to the pump region and the ambipolar diffusion of ions from the pump region to the cell wall. The kinetic processes in K and Rb DPALs considered in the model are presented in the Appendix (section VI).

The flowing-gas K and Rb DPAL properties were based on the model for static K DPAL [1], the difference from [1] was that since the natural convection in fast flowing gas is negligible, the gravity was ignored. The model used the ANSYS FLUENT 3D CFD solver to solve the flow mass, momentum, energy conservation equations and the gaseous species conservation equations. The conservation equations of the FLUENT solver allow for user input to account for the energy transfer and species creation processes in the DPAL medium.

Computations of the dissociative recombination rate constants for alkali ions X_2^+ (X = K, Cs and Rb) were performed using quantum mechanics methods and in particular multi-channel quantum defect theory (MQDT) described in detail in [24].

Calculations of the required potential energy surfaces for the MQDT of K_2 were performed using Molpro quantum chemistry software which is widely used in this field [25]. The MQDT model coupled with Molpro software is applied to calculations of the dissociative recombination cross section of the alkali dimer ions K_2^+ for given kinetic energy of the electron. Averaging of the cross sections over Maxwellian distribution of the electron energy yields dependence of the cross sections on the electron temperature T_e that were used in the kinetic modeling of different DPALs.

Computations of the quenching cross-section of high electronic levels of alkali atoms were performed using quantum mechanics methods. These methods require knowledge of potential energy surfaces for a system consisting of an excited alkali atom and a quenching molecule and the crossing points of these surfaces. First the quenching of the atoms for which the potential energy surfaces are available was studied. Probabilities of transitions between these surfaces were found using the Landau-Zener formula (discussed in item v) of section IV) whereas the quenching cross section was determined by averaging of this probability by the impact parameter and thermal distribution of the initial relative kinetic energy of the alkali atom and the quenching molecule. The details of the calculations are presented below.

The optical model of multi-transverse mode operation is based on calculations of the pump and laser beam intensities in the gain medium, where the laser beam intensity is a linear combination of the azimuthally-symmetric Laguerre-Gaussian modes [26]. In particular, for the donut shaped pump beam, used in the present setup, the output laser beam is composed only from TEM_{0q} modes with zero radial indices [27]. The powers of the pump beam and of the transverse modes are found from the system of differential equations representing the Beer-Lambert law as explained in [26]. The dependence of M^2 on the pump beam diameter can also be obtained using a simple approximate analytical approach to the description of the multi-transverse-mode lasing, similar to that suggested in [28].

IV. Results and discussion

Since the results of items i) - iii) and v) are presented in journal publications, here we provide only the most important results.

i) Dependence of static K DPAL performance on addition of methane: 3D CFD modeling and comparison with experimental results (Ref. 1).

The geometry, gas initial conditions and pump and resonator parameters of the static K DPAL (Fig. 2) were the same as in the experimental setup [13].

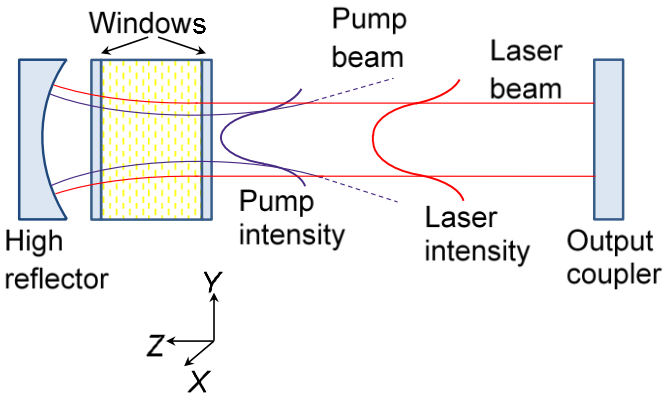

Fig. 2. Schematics of K DPAL studied in [13].

Fig. 3 shows the calculated and measured K DPAL powers, normalized to their maximum values, as a function of partial CH_4 pressure p_{CH4} for three different values of dissociative recombination rate constant k_{24}. For k_{24}= 52.6x10^{-14} m^3/s [18] the laser power is almost independent of p_{CH4} at small p_{CH4} < 100 Torr which is in contrast with the experimental results [13] that show very sharp power increase when p_{CH4} increases from zero to 20 Torr. At the same time for k_{24}=1x10^{-14} m^3/s [19] the calculated power increases very sharply with the addition of ~20 - 50 Torr of CH_4 to pure He buffer gas, the relative increase being ~30%. This behavior of the power is consistent with experimental data [13], although in [13] the increase in power is greater than the calculated one. The main reasons for low power in pure He are slow ion-electron recombination and high electron temperature exceeding 3000 K, resulting in fast ambipolar diffusion of K ions to the wall and depletion of the neutral K atoms in the lasing region. These effects are mitigated when methane is added to the buffer gas leading to the sharp increase in power. A further increase of p_{CH4} leads to a decrease in the laser power for both values of k_{24}, mainly due to the increase of the linewidths of the pump and laser transitions, which cause a decrease in the pump absorption and stimulated emission cross sections.

Thus, the calculated results for the normalized laser power are in satisfactory agreement with the measured values for k_{24} = 1x10^{-14} m^3/s. Larger or smaller values of k_{24} do not reproduce the experimental results.

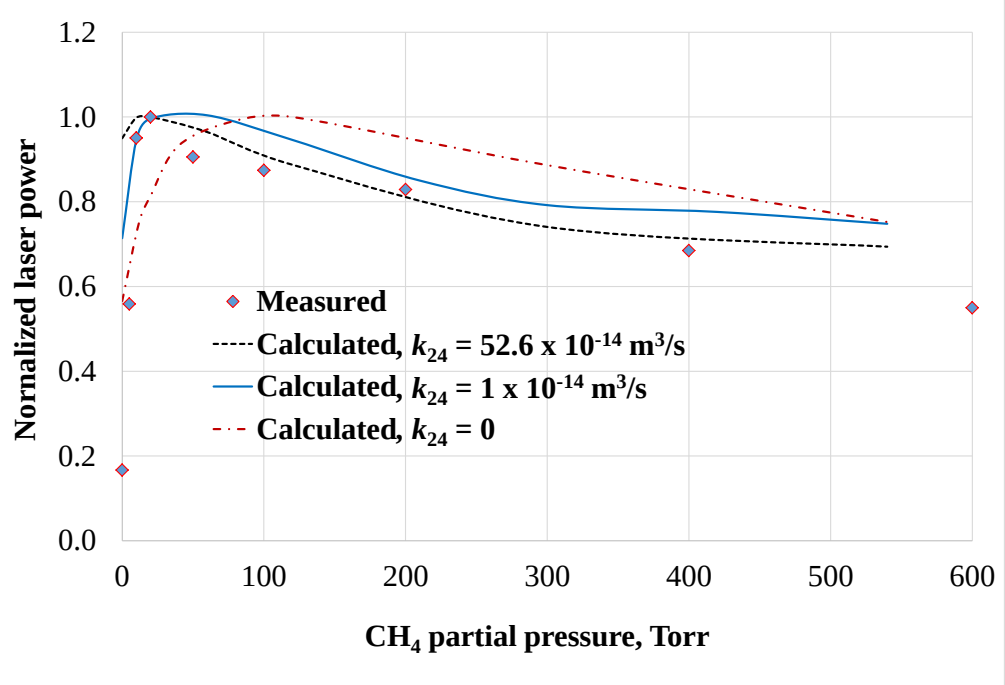

Fig. 3. Calculated and measured power [13] of K DPAL (normalized to the maximum value) as a function of partial CH_4 pressure. Calculations were performed for three values of the dissociative recombination rate constant k_{24}.

ii) Velocity dependence of the performance of flowing-gas K DPAL with He and He/CH_4 buffer gases: 3D CFD modeling and comparison with experimental results (Ref. 2).

Two pumping schemes for the flowing-gas K DPAL were considered. Fig. 4(a) shows the transverse pumping and Fig. 4(b) the end pumping setup. For both schemes the pump beams were Gaussian with the waist at the cell center and the laser beam with a constant cross section in the propagation direction z.

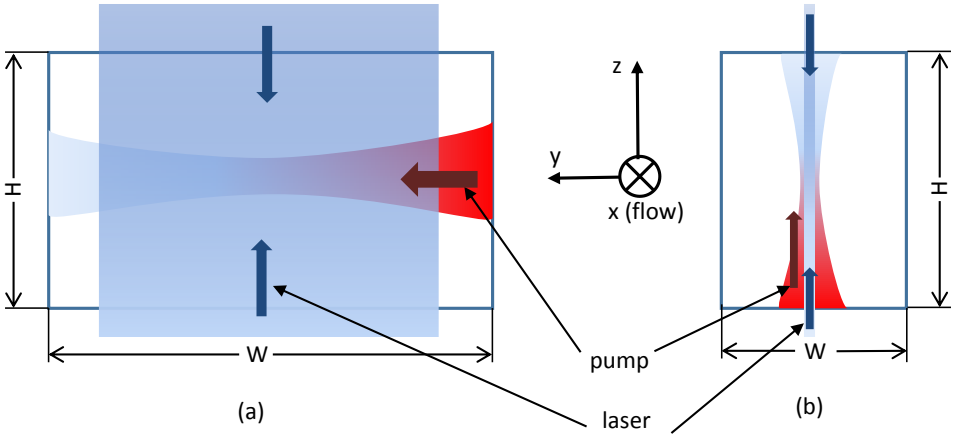

Fig. 4. Transverse (a) and end (b) pumping setup.

Figures 5a and b show the dependence of the laser power on the flow velocity for constant pump power for the transverse and end pump geometries, respectively, and different molar fractions of methane, xCH_4, in the buffer gas.

It is seen that for both geometries the power achieved with pure He buffer gas is much lower than that achieved when methane is added to He. The laser power increases with increasing flow velocity approaching its asymptotic maximum value at very high velocities ~500 m/s. These values are much larger than the value of 100 m/s estimated in [13]. Such high flow velocities can be obtained in the flowing-gas DPAL with pure He buffer gas using sonic or supersonic nozzles suggested in [29-31] where modeling of K flowing-gas DPAL with transverse pump geometry, pure He buffer gas and flow velocities exceeding 1000 m/s was performed. For such high velocities the effects of ambipolar diffusion are not important. It was shown in [31] that for such a laser, applying subsonic, transonic and supersonic flows, the output power can be scaled up to megawatt level with high optical-to optical efficiency exceeding 60% (see Fig. 5).

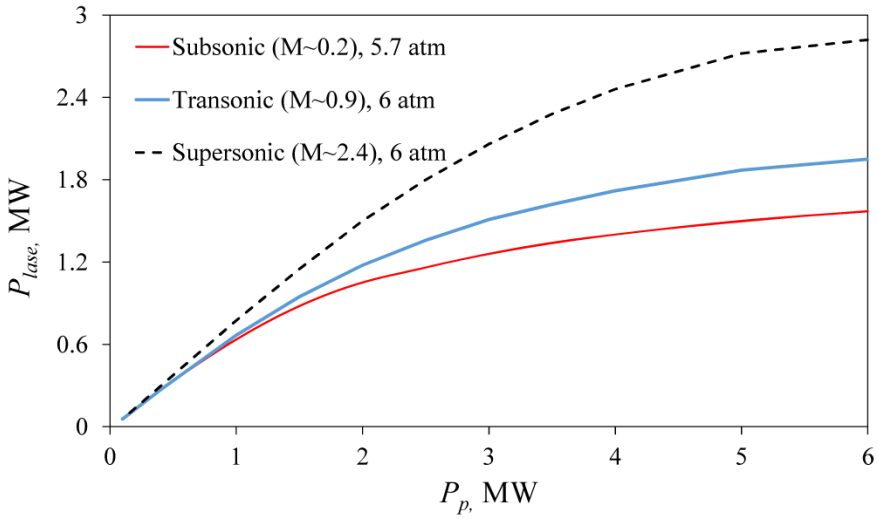

Fig. 5. Dependence of the laser power, P_{lase}, on the pump power, P_p, for subsonic (M ~ 0.2) transonic (M ~ 0.9) and supersonic (M ~ 2.4) K DPALs with He as a buffer gas [31].

At the same time adding methane to He results in much lower velocities required to achieve the maximum possible power. For example, at $xCH_4 = 0.4$ this velocity is ~10 m/s (see Fig. 6). Fig. 5a also shows the dependence of power on flow velocity for the transverse pumping scheme at 0.0176 molar fraction of methane used in the experiments [15]. It is seen that power exceeding 90% of the maximum value is achieved at flow velocity of 40 m/s which is much higher than 3.9 m/s applied in [15].

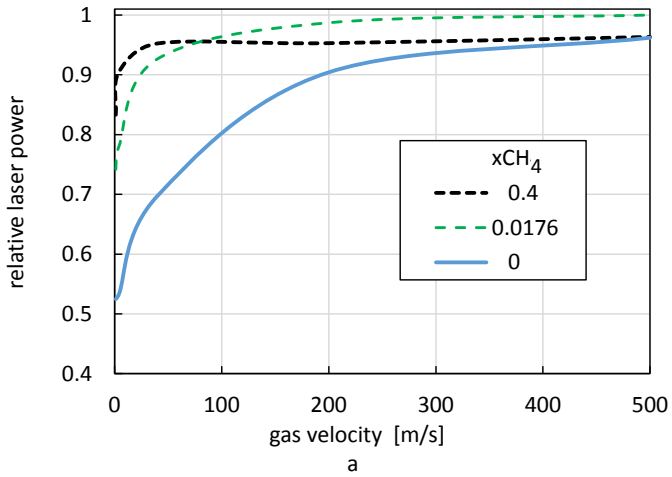

a

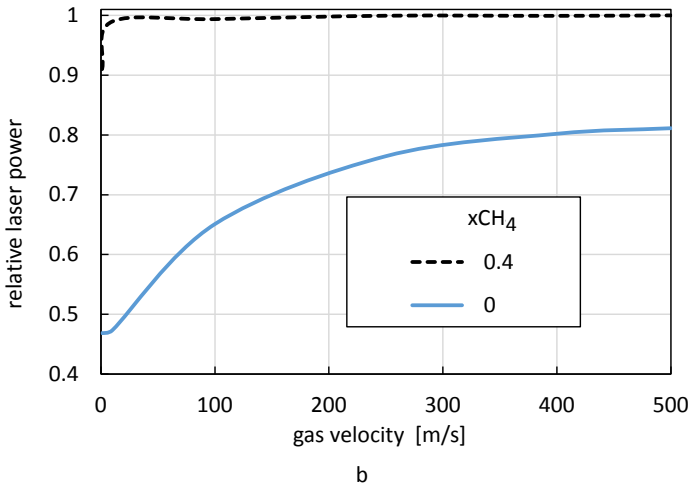

Fig. 6. Dependence of the relative laser power on the flow velocity for the transverse pump (a) and end pump (b) geometries and different molar fractions of methane, xCH_4, in the buffer gas. The pump power is 1600 W and 600 W for (a) and (b), respectively. The laser power in (a) and (b) is related to the maximum values of 100.4 W and 55 W, respectively. Methane molar fraction of 0.0176, shown in (a), was used in [15].

Fig. 7 shows the calculated and measured [15] dependence of the laser power on the pump power for the transverse pumping geometry and different molar fractions of methane in the buffer gas. For the methane molar fraction of 0.0176 the agreement between the measured and calculated values is satisfactory. For pure He the calculated power decreases by ~30% which is consistent with experimental data, although the measured decrease in power is greater than the calculated value.

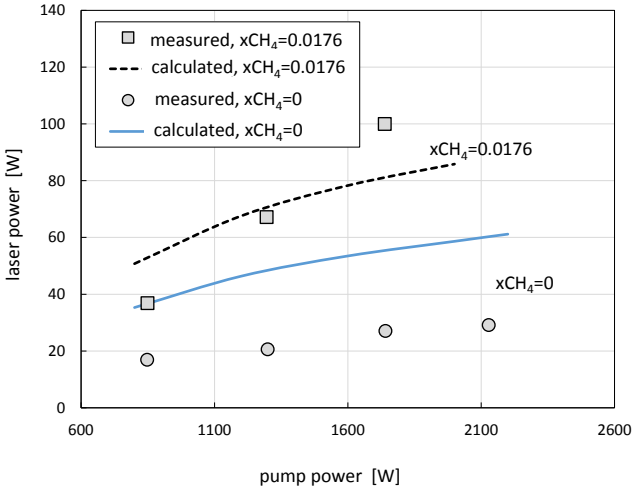

Fig. 7. Measured and calculated dependence of the laser power on the pump power for the transverse pumping geometry [15] and different molar fractions of methane.

iii) 3D CFD modeling of flowing-gas Rb DPALs: effects of buffer gas composition and of ionization of high lying Rb states (Refs. 3 and 4).

The end pumping scheme for the flowing-gas Rb DPAL shown in Fig. 8 was considered. The DPAL cell is a rectangular box with the laser and pump beams propagating in the z direction, L_z is the gain length and also the flow channel width. The flow is in the x direction perpendicular to the pump and laser direction, the flow channel height is L_y and the length in the flow direction is L_x. The lasing medium consisted of a mixture of Rb vapor and He/CH_4 buffer gas with given conditions at the entrance to the laser cell: pressure p, temperature T, velocity u and Rb number density N_{Rb}. The cell walls and windows temperature, T_w, was higher by 10°C than the gas temperature.

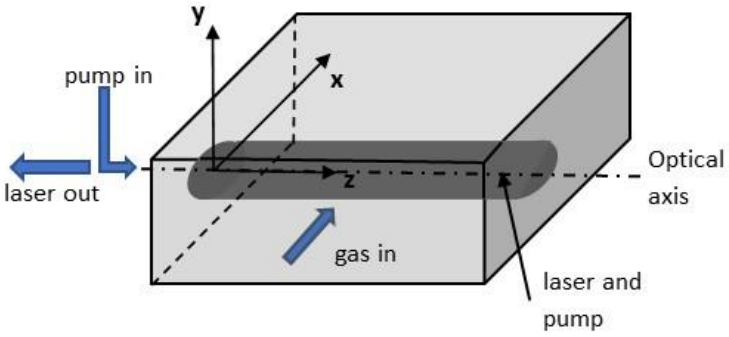

Fig. 8. End pumping setup for the flowing-gas Rb DPAL. The flow is in the x direction perpendicular to the pump and laser direction.

A detailed list of the considered kinetic processes and the corresponding rate constants are presented in Refs. 3 and 4. The calculations were performed for two types of Rb DPAL. The first is a low-power laboratory-scale device with pump power of several tens of W and the second is a high-power multikilowatt laser.

For the low power device, the gas mixture conditions at the DPAL cell entrance and the optics data are presented in Refs. 3 and 4. The DPAL cell dimensions are $L_x = L_z = 1.5$ cm, $L_y = 1$ cm.

Figure 9 shows the pump intensity spatial distribution in the gain volume in the y-z plane containing the optical axis. It can be seen that the pump beam is completely absorbed in the gain medium.

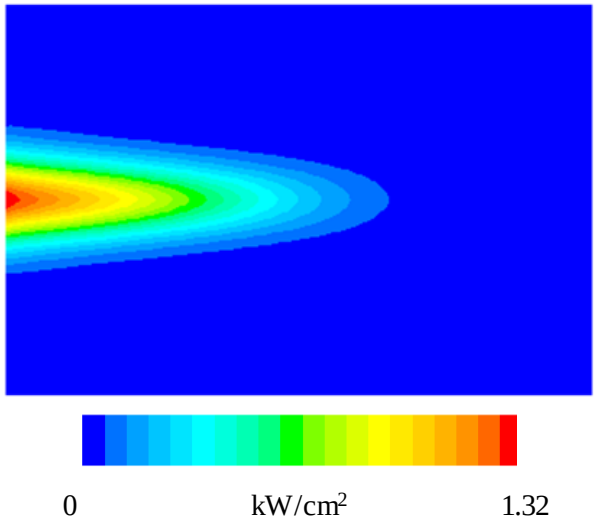

Fig. 9. Spatial distribution of the pump intensity in the gain volume in the y-z plane containing the optical axis at a flow velocity of 1 m/s and pump power of 30 W.

Figures 10 and 11 show the spatial distribution of the gas flow velocity and temperature in the x-y plane in the middle of the flow channel; in these figures the gas flows from left to right. The gas velocity increases along the flow due to friction with the channel walls and heat absorption, while the maximum temperature is reached in the middle of the cell, where the flow crosses the pump beam and the laser beam.

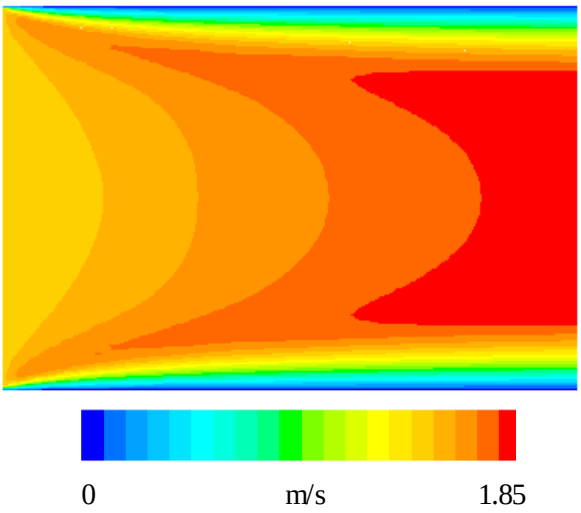

Fig. 10. Spatial distribution of gas flow velocity in the x-y plane in the middle of the flow channel, flow from left to right at a flow velocity of 1 m/s in the inlet and pump power of 30 W.

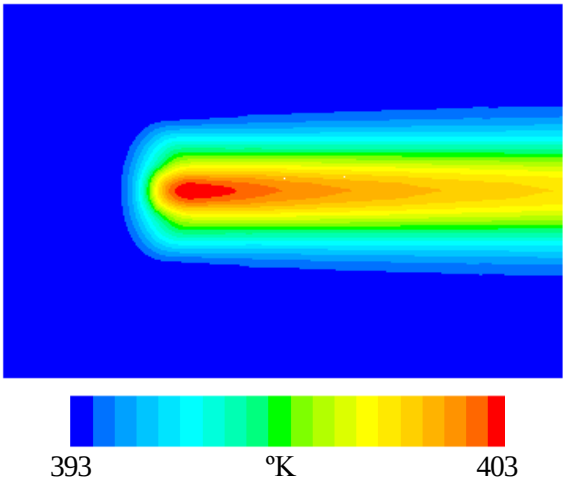

Fig. 11. Spatial distribution of the gas temperature in the x-y plane in the middle of the flow channel, flow from left to right at a flow velocity of 1 m/s in the inlet and pump power of 30 W.

Figure 12 shows the dependence of the laser power on the molar fraction of CH_4 for several values of the inlet gas pressure. For each pressure value there is an optimal CH_4 molar fraction corresponding to the maximum laser power. E.g., at 1 atm the maximum power is reached at CH_4 molar fraction of 0.5. Note that the power achieved with pure He buffer gas is much lower than that achieved when methane is added to He. The reason is that in pure He, where the relaxation rate is low, the pump power of 30 W is close to the threshold. Therefore, efficient operation of Rb DPAL with pure He buffer gas is only possible at a significantly higher pump power. In the entire range of methane mole fractions, the laser power decreases with increasing pressure, and the maximum power is attained at atmospheric pressure.

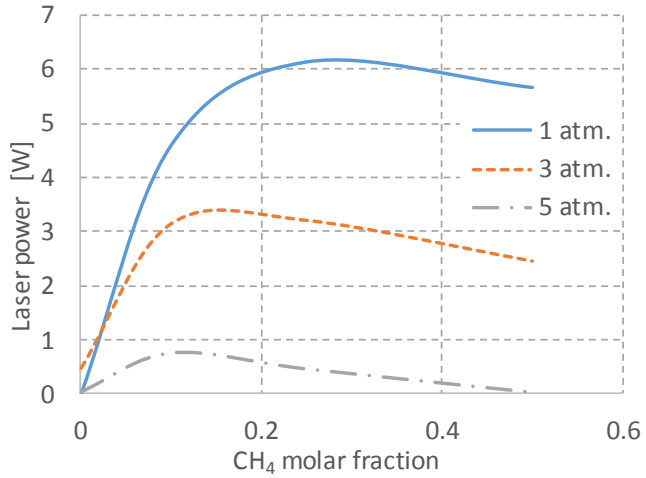

Fig. 12. Laser power as a function of CH_4 molar fraction for several gas pressures and flow velocity of 2 m/s in the inlet and pump power of 30 W.

Our calculations showed that in a low-power device with pumping power of ~ 30-40 W it is possible to obtain output power of several watts at optimal buffer gas pressure of 1 atm and methane mole fraction of 0.25.

To achieve high multi-kilowatt power, it is necessary to avoid saturation of the D_2 pump transition. For this, the transverse radii of the pump and laser beams were increased to 2.5 mm. The gas mixture conditions at the DPAL cell entrance and optical data are presented in Refs. 3 and 4. The DPAL cell dimensions are L_x = 3 cm, $L_y = L_z$ = 2 cm.

Fig. 13 shows the dependence of the laser power on the pump power. The solid line shows the power calculated using the full model which considers the excitation of high levels and ionization of Rb atoms; the dashed line shows the power calculated using the three-level model, which does not consider these processes. The laser power calculated using the full model agrees with that calculated using the three-level model for pump power less than ~ 15 kW. However, at higher pump power the processes of high-level excitation and ionization lead to a twofold decrease in the maximum attainable laser power in comparison with the power calculated using the three-level model.

Fig. 14 shows the dependence of the laser power on methane molar fraction in the methane/He buffer gas for two gas pressures, 1.5 and 5 atm. The laser power rapidly decreases with decreasing molar fraction of methane.

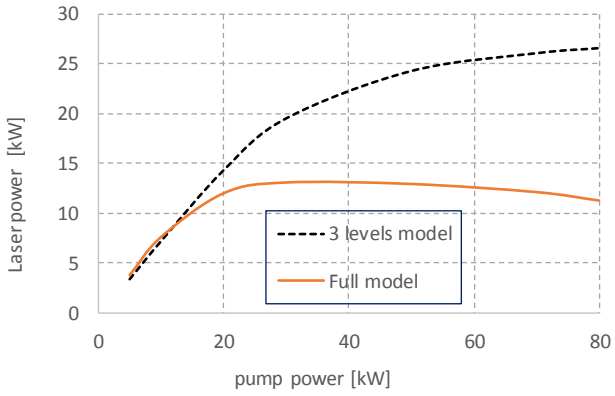

Fig.13. Laser power as a function of pump power calculated using the full model and the three levels model.

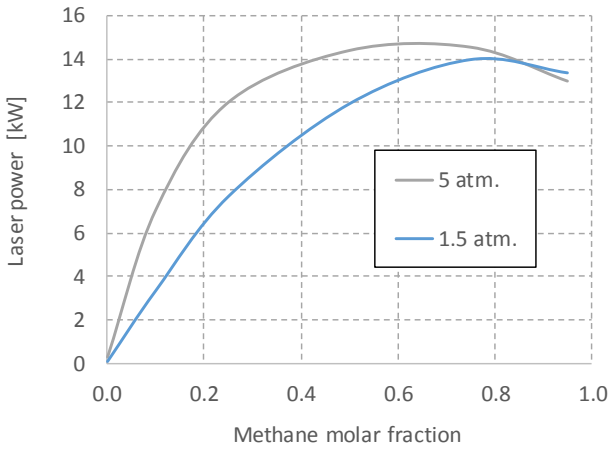

Fig. 14. Laser power as a function of methane molar fraction for several buffer gas pressures for 20 kW pump power.

As shown in Fig. 14, efficient operation of Rb DPAL with pure He buffer gas is not possible under the current conditions. This is because at pump intensity of 100 kW/cm^2 (corresponding to a power of 20 kW), the pump transition is highly saturated due to the low relaxation rate of the fine structure levels of Rb atoms. To increase the laser efficiency and power the pump intensity in the laser with pure He buffer gas should be reduced to ~50 kW/cm^2. For this purpose, in the case of a pure He buffer gas, we performed calculations for a larger cross-sectional area of the pump beam, 5 cm^2. We compared the results of the present model and the results obtained in Ref. 22 where a simplified three-level model based on the 1D gas dynamics approach was employed.

Figure 15 shows the dependence of the laser intensity on the pump intensity for Rb DPAL with pure He buffer gas for two flow velocities. The laser radiation intensity calculated by our model agrees with that obtained in Ref. 22 for pump intensities less than ~ 15 W/cm^2; however, for higher pump intensities, when the D_2 pump transition is saturated, the laser intensity calculated using our model is much lower than that calculated in Ref. 22 for two different values of the flow velocity v. The reason for this difference is that the processes of excitation of high levels of Rb and its ionization result in strong energy losses in the laser gain medium.

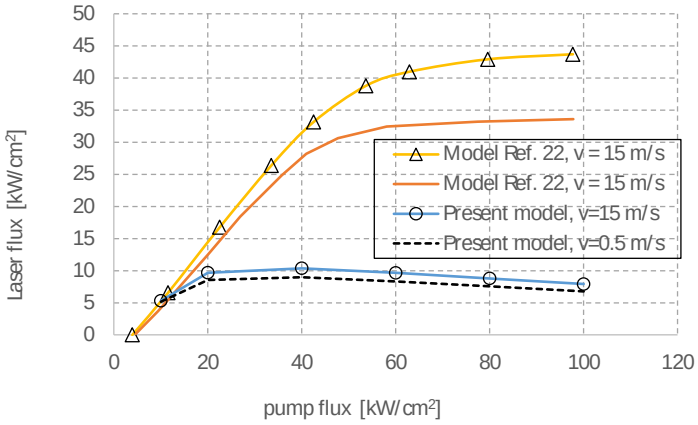

Fig. 15. Laser intensity as a function of pump intensity in Rb DPAL with pure He buffer gas for the present model and the 1D three-level model[8] at different flow velocities. Optical and flow conditions are the same as in Table 3.1 from Ref. 22; in particular, the He pressure is 15 atm.

v) Quantum mechanical computations of the dissociative recombination rate constant of K_2^+ ions in the gain medium of K DPAL: calculations of the potential energy surfaces for highly excited dissociative states of K_2, the ground state of the molecular ion K_2^+ and their crossing points.

As mentioned in section III, computations of the dissociative recombination (DR) rate constants and cross-sections for alkali ions X_2^+ (X = K, Cs and Rb) were performed using quantum mechanics methods and in particular multi-channel quantum defect theory (MQDT). This method requires preliminary knowledge of the potential energy surfaces of the ground state of the molecular ion, highly excited dissociative states of the alkaline molecule itself and their crossing points.

It is important to note that DR calculations use diabatic states, not adiabatic states, which Molpro calculations are optimized for. In Ref. 32 it was stated that one can approximate diabatic calculation by omitting diffuse characters in the basis set. Hence, calculations were carried out using the correlation consistent polarized valence quadrupole-zeta (cc-p VQZ) basis set. The ground state potential energy surface of the molecular ion K_2^+ was carried out using full configuration interaction (FCI) calculation. The active space was made by 14 σ orbitals, six π orbitals and two δ orbitals. All orbitals except the last two σ orbitals, the last two π orbitals and δ orbitals were fully occupied. It is important to mention that Molpro uses an abelian point group symmetry system for calculations. But the point group $d_{\infty h}$ of the diatomic molecules consisting of

the like atoms is non abelian. Hence, for calculations the input symmetry was d_{2h}. Therefore, there would be some states with the same d_{2h} symmetry but with different $d_{\infty h}$ symmetry. For example, A_g states correspond to both Σ states and Δ states. Identification of the corresponding $d_{\infty h}$ states is yet to be accomplished. Calculation of the first six ${}^3B_{2g}$ (which are also energetically equivalent to ${}^3B_{3g}$) dissociative states were performed using FCI calculations as well. The potential energy surfaces are shown in Fig. 16:

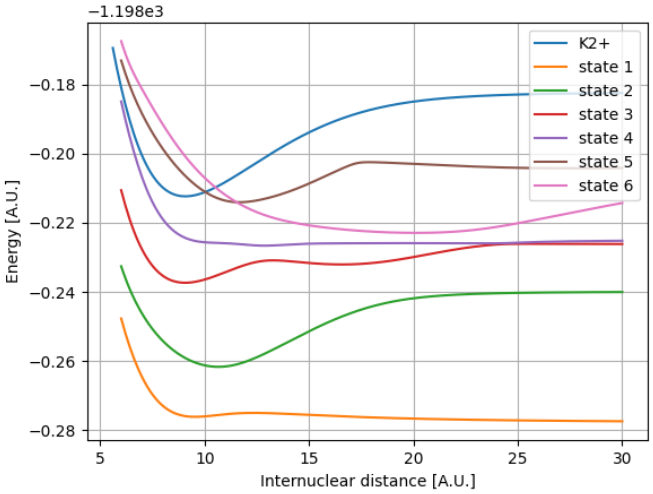

Fig. 16. First six ${}^3B_{2g}$ states.

In addition, the first eight ${}^3B_{1u}$ states have also been calculated. The results are presented in Fig. 17:

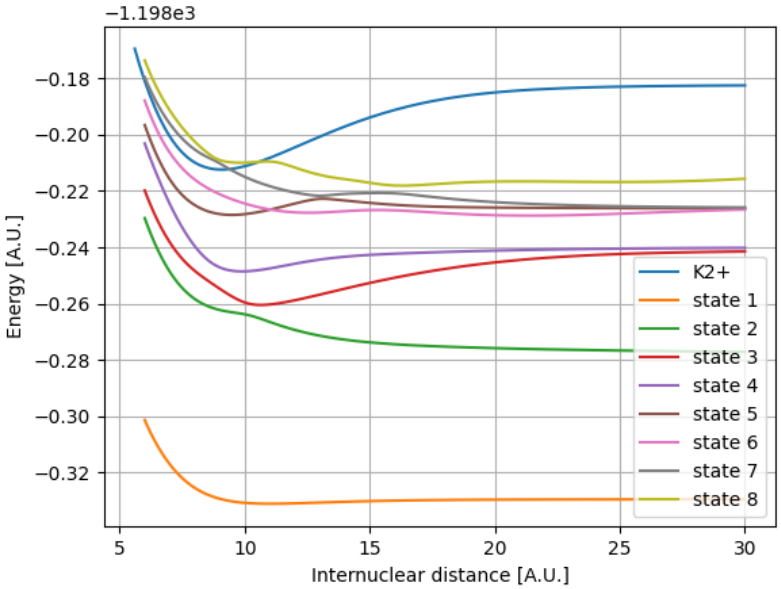

Fig. 17. First eight ${}^3B_{1u}$ states.

Furthermore, the first six ${}^3A_g$ states have also been calculated. The results are shown in Fig. 18:

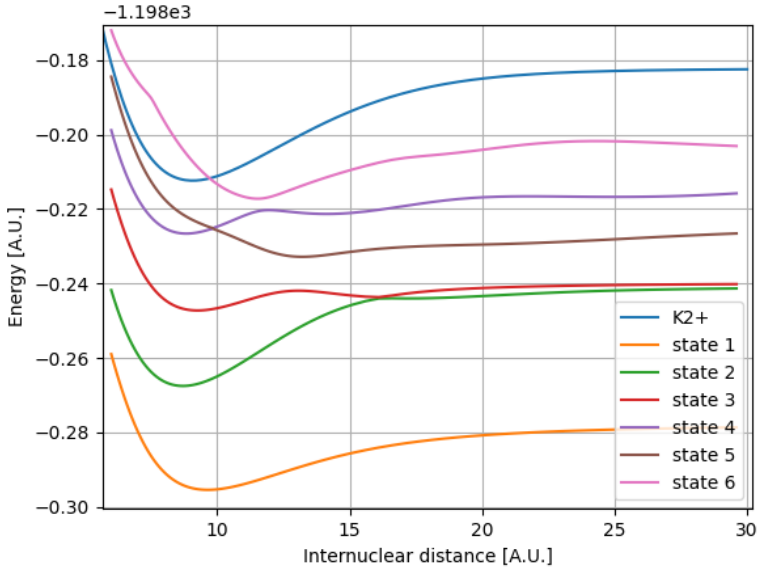

Fig. 18. First six ${}^3A_g$ states.

It is important to note that the atomic states which the molecule dissociates to have yet to be determined and will be studied in further research.

Accuracy of the calculations. The ground state molecular ion K_2^+ potential energy calculation is quite accurate in comparison with previous work [33], as can be seen in Fig. 19.

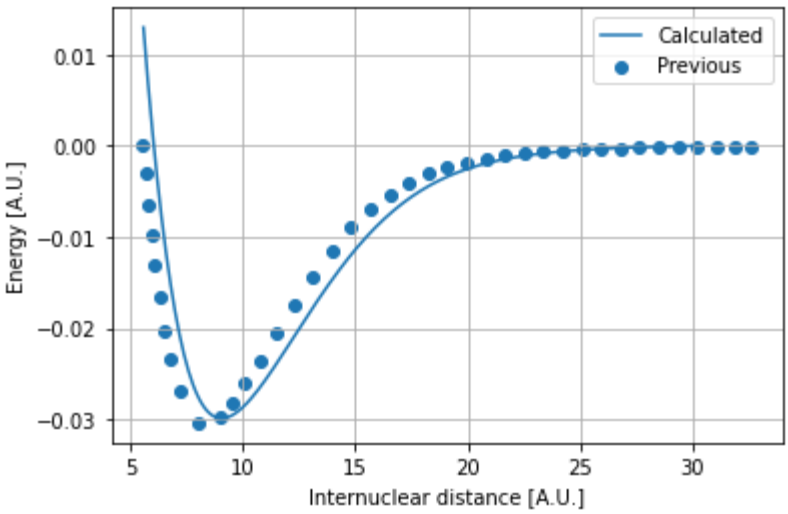

Fig. 19: K_2^+ ground state potential energy calculation compared to previous work [33].

As for the excited states, a similar calculation was performed in [32] using Molpro for CO dissociative recombination. The Molpro algorithm which was used in [32] was replicated so it could be applied for the calculations of K_2. The algorithm uses the MRCI (multireference configuration interaction) method. The results for the first five $^3B_{2g}$ states using the replicated algorithm, compared to previous FCI calculations, are shown in Fig. 20:

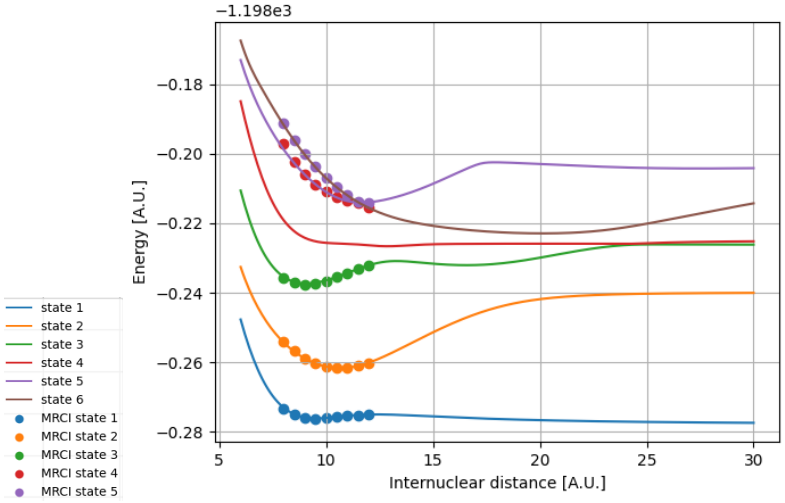

Fig. 20. MRCI results for the first five $^3B_{2g}$ states.

It appears that when applying this algorithm to K_2, it does not converge at longer internuclear distances. Moreover, at the distances at which the calculations converge, the MRCI calculations agree fairly well with the FCI calculations. Hence, we can conclude

that the FCI calculation is more accurate and easier to implement because it does converge at longer distances. It is worth noting that the common convention in the literature [34] is that the FCI method with complete basis set is regarded as the exact solution. Therefore, at this stage it is safe to assume that FCI describes the excited state with sufficient accuracy for use in calculation of DR.

We note in passing that the replicated algorithm's result misses the fourth excited state entirely. On the contrary the FCI seems to calculate it reasonably, further indicating the validity of FCI calculation in our case.

v) Calculations of the quenching cross-section of the excited electronic levels of Rb by methane using quantum mechanics methods.

Excitation and ionization of high electronic levels of alkali atoms ($nP_{1/2,3/2}$, $(n+1)P_{1/2,3/2}$, $(n+2)S_{1/2}$ and $nD_{3/2,5/2}$, where n = 4, 5, 6 for K, Rb and Cs, respectively) and their quenching by different buffer gas molecules (these processes are depicted in Fig. 1) strongly affect the DPAL operation at high laser and pump powers. We have carried out computations of the quenching cross-section of these levels using quantum mechanics methods. First, the quenching of $6P_{1/2,3/2}$ level of Rb atom by CH_4 molecule was studied. This pair was chosen because the quenching cross section for it was measured in [35, 36] and since the calculated potential energy surfaces are available [35].

Potential energy curves for Rb atom approaching CH_4 along a H-CH_3 bond axis (end-on approach), where Rb atom is in different electronic states and CH_4 in different vibrational levels (v=0,1) as a function of the distance R between the species are shown in Fig. 21. The curves for v=0 are taken from [35,37] whereas to calculate the potential curves for higher vibrational levels, v>0, we displaced them in energy by the vibrational spacing of CH_4, as recommended in Refs. [38,39].

The quenching process includes approaching of the atom to the molecule, electronic transition between the potential curves corresponding to different electronic states of Rb and vibrational states of CH_4 at infinite distance R and separation of the species. The probability of the electronic transition between the potential energy curves is large (~1) only if there are crossings between the curves, resulting in quenching cross section larger than the gas-kinetic value [40]. If there is no crossing the probability is exponentially smaller [40]. As seen in Fig. 21, the only crossing of the potential curves is that of curves 1 and 2 at a distance R_c = 5 Å. Here curve 1 describes potential energy of Rb(6P) and unexcited CH_4(v=0), whereas curve 2 – potential energy of Rb(6S) and vibrationally

excited C—H stretching mode of CH_4 with v=1. That means that Rb(6P) is quenched mainly to Rb(6S) with vibrational excitation of the stretching of CH_4. The quenching to other states and in particular to 4D state has much smaller cross section.

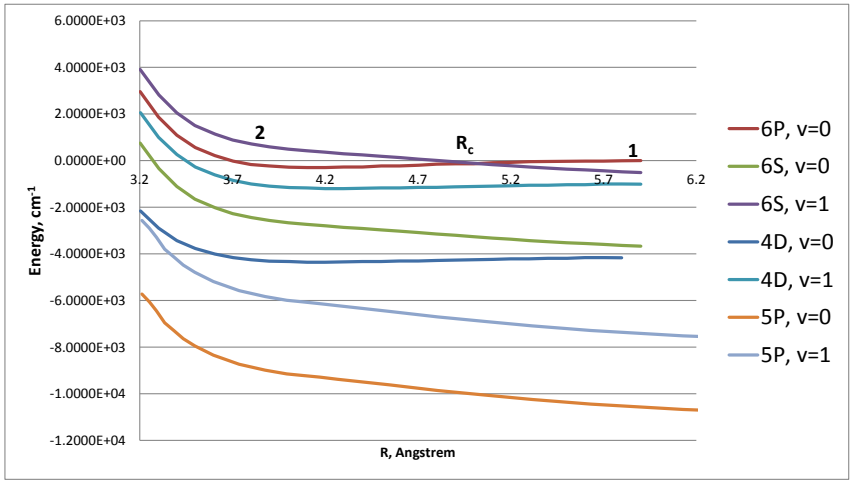

Fig. 21. Potential energy curves for the end-on approach of Rb to CH_4. The curves for v=0 are taken from [35,37] whereas to calculate the potential curves for higher vibrational levels, v>0, we displaced them in energy by the vibrational spacing of CH_4, as recommended in Refs. [38,39].

The quenching cross section has been estimated using the modified approximated formula of Landau, taking into account both electronic and vibrational transitions [38-40]:

$$\sigma_q = \pi R_c^2 \frac{4V_{el}^2(R_c)q_{01}}{\hbar|F_2 - F_1|}\frac{\sqrt{2\mu[E - U(R_c)]}}{E}, \qquad (1)$$

where $V_{el}(R_c)$ is the simple Landau-Zener electronic interaction matrix element, q_{01} is the Franck-Condon vibrational overlap integral for the transition v=0→v=1 of CH_4 stretching mode, $F_{1,2} = -\frac{dU_{1,2}}{dR}(R = R_c)$, $U_{1,2}$ are the potential energies of curves 1 and 2, respectively, μ is the reduced mass of Rb and CH_4, E is the total kinetic energy of Rb and CH_4 at the infinite distance and $U(R_c)$ is the common value of U_1 and U_2 in the crossing point R_c. Averaging of σ_q over E using Maxwell distribution of the energies at the gas temperature $T >> U(R_c)/k$ (which is the case for T~400 K used in Rb DPALs) led to the following very simple approximate expression for $\sigma_q(T)$:

$$\sigma_q = \pi R_c^2 \frac{4V_{el}^2(R_c)q_{01}}{\hbar|F_2 - F_1|\sqrt{\frac{\pi}{8}\frac{kT}{\mu}}}, \qquad (2)$$

where *k* is the Boltzmann constant. The parameters R_c and $F_{1,2}$ in Eq. (2) were estimated using potential curves shown in Fig. 20, whereas $V_{el}(R_c)$ using the correlation suggested in Ref. [39]. The Franck-Condon factors were estimated using Morse potential approximation with the displaced equilibrium positions of the atoms in CH_4, the value of q_{01} being ~0.015. For these values of the parameters at *T*= 350 K we got the value of σ_q = 71 Å^2 being in satisfactory agreement with the measured value of 84 Å^2 [35]. Such an agreement is surprisingly good taking into account the rough approximations used in the computations.

Accurate value of σ_q without the aforementioned approximations was found by using the Landau-Zener equation for the transition probability between the crossing potential curves [40]:

$$P = 2\exp\left(-\frac{2V_{el}^2(R_c)q_{01}}{\hbar|F_2 - F_1|v}\right)\left[1-\exp\left(-\frac{2V_{el}^2(R_c)q_{01}}{\hbar|F_2 - F_1|v}\right)\right], \quad (3)$$

where the relative velocity *v* of Rb atom and CH_4 molecule in the curve crossing point R_c is given by:

$$v = \sqrt{\frac{2\left(E - U(R_c) - \rho^2 E/R_c^2\right)}{\mu}} \quad (4)$$

and ρ is the impact parameter. Then the quenching cross section σ_q averaged over the thermal distribution of *E* is given by the following expression:

$$\sigma_q = \int_0^\infty dE\, 2\sqrt{\frac{E}{\pi(kT)^3}}\exp(-E/kT)\int_0^{\sqrt{[1-U(R_c)/E]}R_c} 2\pi\rho d\rho P(E,\rho). \quad (5)$$

Using the aforementioned parameters and performing integration in Eq. (5) we got σ_q = 56 Å^2. This value is lower than σ_q = 71 Å^2 obtained from the analytical formula (2) but anyway is in satisfactory agreement with the measured value of 84 Å^2 [35].

vi) Detailed theoretical study of controlling the beam quality in DPALs by changing the resonator parameters (Refs. 5 and 6).

Schematics of the flowing-gas Cs DPAL with end-pumping geometry is depicted in Fig. 22.

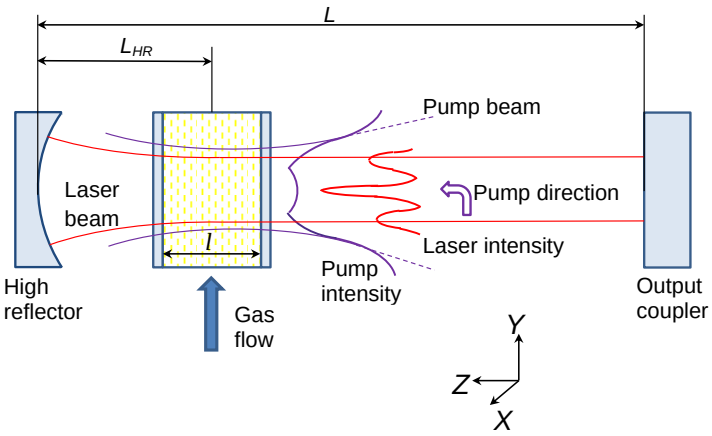

Fig. 22. Schematics of the flowing gas Cs DPAL with end-pump geometry. Pump beam of circular symmetry and with a donut-shaped intensity profile was used.

Figure 23 shows calculated M^2 dependence on the average laser beam diameter $\bar{d}$ over the laser cell. It is seen that for small $\bar{d} \sim 0.6$ mm the values of M^2 are large (10–16). As $\bar{d}$ is increased to 1.5-2 mm and approaches the pump beam diameter, M^2 drops to much smaller values, < 2, resulting in significant improvement of the laser beam quality.

The circles and triangles in Fig. 23 show the experimental results. As seen in Fig. 23, good agreement is obtained between calculated and measured values of M^2.

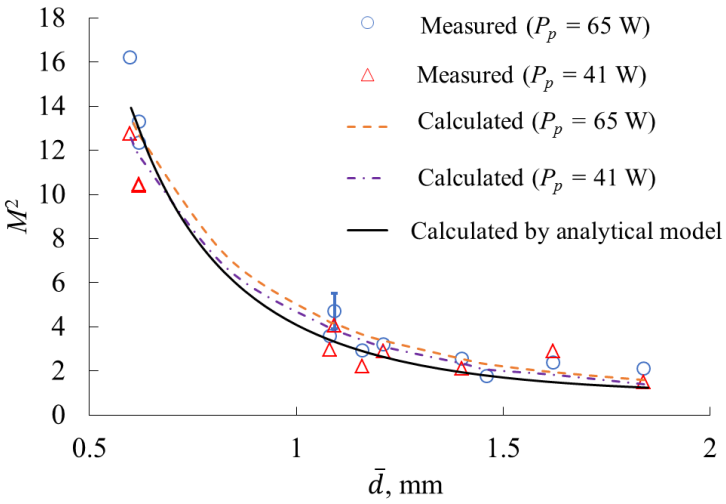

Fig. 23. Measured and calculated (by optical model of multi-transverse mode operation) dependence of the laser beam qualityM^2 on the average laser beam diameter $\bar{d}$ for the pump powers P_p = 65 W and P_p = 41 W. As $\bar{d}$ approaches the size of the pump beam diameter, the laser operation approaches the single-mode regime.

Using the above-mentioned multi-mode model, we can evaluate the number of transverse modes participating in lasing for given P_p and $\bar{d}$. Fig. 24 shows the calculated power distribution over the laser transverse-modes for P_p = 65 W and three different values of $\bar{d}$: 1.84 mm (M^2 = 1.63), 1.1 mm (M^2 = 4.16) and 0.6 mm (M^2 = 13.62). It is seen that in the case of the largest M^2, 10 transverse-modes oscillate, the highest-order mode number being 30. At the same time in the smallest M^2 case, only two lowest order modes oscillate resulting in the aforementioned nearly single mode laser operation.

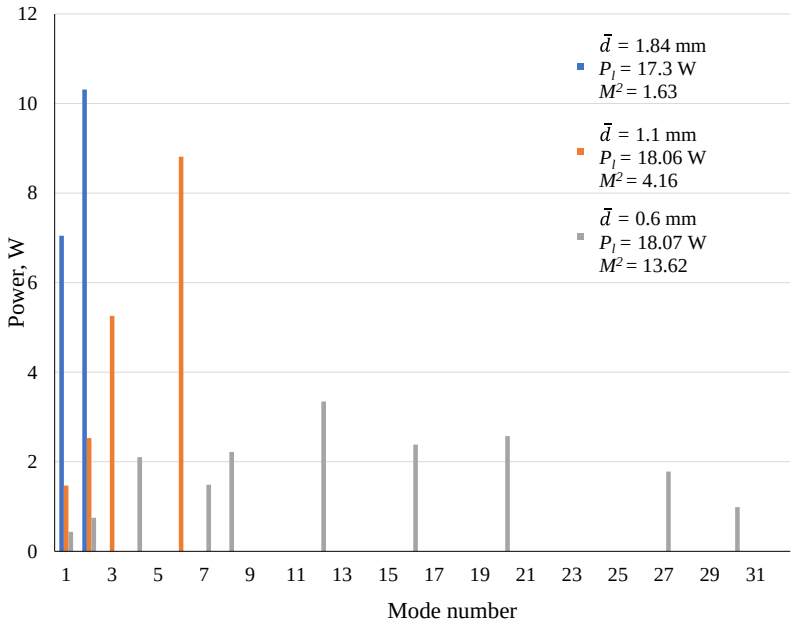

Fig. 24. Laser modal composition for 3 cases of $\bar{d}$, calculated by multi-transverse-mode model [26,27]. For the values of $\bar{d}$ corresponding to large laser beam quality M^2 (grey bars), 10 transverse-modes lase, the highest-order mode number being 30. For the smallest M^2 case (blue bars), only the two lowest order modes lase.

The dependence of M^2 on $\bar{d}$ can also be obtained using a simple approximate analytical approach to the description of the multi-transverse-mode lasing, similar to that suggested in [28]. Although this approach is inaccurate, it predicts the correct scaling law for the decrease of M^2 with increasing $\bar{d}$. Figure 23 shows the analytical dependence of M^2 on $\bar{d}$. The calculated results are in good agreement with the measured values.

V. Conclusions

i) The 3D CFD model, supplemented by the analysis of the electron temperature, and applied to the computations of the laser power of static K DPAL, explains the sharp

increase in power caused by the addition of a few percent of methane to He buffer gas and its decrease with further increase in the methane percentage. The main reasons for low power in pure He are slow ion-electron recombination and high electron temperature exceeding 3000 K, resulting in fast ambipolar diffusion of K ions to the wall and depletion of the neutral K atoms in the lasing region. These effects are mitigated when methane is added to the buffer gas. The calculated results for the normalized laser power are in satisfactory agreement with the measured values for a rate constant of the dissociative recombination of $1x10^{-14}$ m^3/s. Larger or smaller values of this rate constant do not reproduce the experimental results.

ii) An accurate 3D CFD modeling of the flowing-gas K DPAL showed that for low flow velocities, < 10 m/s, just as in the case of the static laser, the laser power achieved with pure He buffer gas is much lower than in the case when methane is added to He. Dependence of the power on the flow velocity was calculated and it was found that with pure He buffer gas the lowest flow velocity required for efficient laser operation is ~500 m/s, and is much higher than the 100 m/s estimated in [11], for both end and transverse pump geometries. High flow velocities can be obtained in the flowing-gas DPAL using sonic or supersonic nozzles suggested in [29-31], where it was shown that for such a laser the output power can be scaled up to megawatt level with high optical-to optical efficiency exceeding 60%.

The calculated power for the transverse pumping and small molar fraction of methane in the buffer gas is in satisfactory agreement with the power measured in [15]. For pure He buffer gas the power decreases by 30% which is consistent with the experimental data [15].

iii) A comprehensive three-dimensional modeling of flowing-gas Rb DPAL was performed. The cases of He/CH_4 and pure He buffer gases were investigated and the output power and optical efficiency calculated for various pump powers, mole fractions of methane, buffer gas pressures and flow velocities. The model considers the processes of excitation of high levels of Rb, ionization, ion-electron recombination and heating of electrons which affect the diffusion coefficient of Rb ions. Two types of Rb DPAL were studied: a low-power laboratory-scale device with pump power of several tens of W and a high-power multi-kilowatt laser. Three-dimensional spatial distributions of the pump power, flow velocity, and temperature were found, as well as the dependence of the laser

output power on various parameters. It was found that using the low-power device it is possible to get output power of several watts for the optimal buffer gas pressure of 1 atm and methane molar fraction of 0.25. Efficient operation of a compact multi-kilowatt device with a pump beam radius of <0.5 cm is possible only for buffer gas containing methane, where its optimal molar fraction is ~ 0.5-0.8. The processes of high-level excitation and ionization lead to a twofold decrease in the maximum attainable laser power in comparison with the power calculated using the three-level model which does not take into account the excitation and ionization processes.

To ensure efficient operation of a laser using pure helium as buffer gas, it is necessary to reduce the intensity of the pump beam in order to avoid saturation of the D_2 pump transition. This can be achieved only in a large-scale laser with a pump beam cross-sectional area of several cm^2. The calculated results for such a device were compared with the results obtained in [22] using a simplified three-level model based on 1D gas dynamics approach. Our model predicts a lower intensity of laser radiation than the 1D three-level model [22]. The reason for this difference is that the processes of excitation of high levels of Rb and its ionization result in strong energy losses in the laser gain medium. As a result, the output power and optical efficiency of the laser, calculated using our model, were approximately 2-3 times lower than those calculated using the 1D three-level model [22].

iv) Dissociative recombination of the alkali dimer ions strongly affects the output power of K DPAL with pure He buffer gas. Literature search showed that calculations of the dissociative recombination rate constants should be performed using MQDT model coupled with Molpro quantum chemistry software [25] for calculation of potential energy surfaces of the ground state of the molecular ion, highly excited dissociative states of the alkaline molecule itself and their crossing points. Computations of the potential energy surfaces are completed, whereas calculations of the dissociative recombination rate constants are underway.

v) Quenching cross-sections σ_q of the high electronic levels $n^2D_{3/2,5/2}$, $(n+1)^2P_{3/2,1/2}$ and $(n+2)^2S_{1/2}$ of alkali metals (where n = 4, 5, 6 for K, Rb and Cs, respectively) can be calculated by finding the crossing points of the potential curves of the initial and final states and employing Landau-Zener equation averaged over the thermal distribution of the total kinetic energy of the atom and quenching molecule at infinite distance. Calculation

of σ_q for $6^2P_{3/2,1/2}$ state of Rb atom shows that this state is quenched mainly to $6^2S_{1/2}$ state with vibrational excitation of the stretching of CH_4. Calculated value of σ_q, 56 Å^2, is in satisfactory agreement with the measured value of 84 Å^2 [35].

vi) The dependence of the beam quality factor M^2 in flowing-gas Cs DPALs with stable optical resonators on the resonator geometry was studied theoretically. Conditions for nearly single mode laser operation resulting in substantial improvement of the output laser beam quality, reducing M^2 close to unity, were found. The beam quality of the output laser beam can be controlled by changing the length of the resonator, and/or the radius of curvature of the high reflection mirror, leaving all other parameters of the laser unchanged. The calculated M^2 values using both the optical model of multi-transverse mode operation [26] and a simple analytical method similar to that suggested in [28] are in agreement with the measured values. Note that accurate values of M^2 were obtained using the multimode model while analytical formula provides for only a scaling law $M^2 \sim \bar{d}^{-2}$ at large M^2 and can be used for rough estimates of the output beam quality in DPALs with stable resonators.

VI. Appendix: kinetic processes in K and Rb DPALs

Kinetic processes and their rate constants in K and Rb DPALs are presented in Tables 1 and 2, respectively.

Table 1. Kinetic processes in K DPAL, baseline rate constants. ν_p and ν_l are the frequencies of the pump and laser transitions, respectively, and e and e_{hot} designate electron with low and high kinetic energy, respectively. The rate constants and cross sections used in [30] are given without references; for the remaining constants, the values found in other references indicated in the table are used.

No.	Process	Cross section	Rate constant
	Pumping		
1	$K(4^2S_{1/2}) + h\nu_p \rightarrow K(4^2P_{3/2})$		
	Relaxation		
2	$K(4^2P_{3/2})+M \rightarrow K(4^2P_{1/2})+M$	17.8 Å^2 (He) 58 Å^2 (CH_4)	Rate constant equals to cross section multiplied by the average thermal velocity
	Lasing		
3	$K(4^2P_{1/2}) + nh\nu_l \rightarrow K(4^2S_{1/2}) + (n+1)h\nu_l$		

	Spontaneous emission		
4	$K(4^2P_{3/2}) \rightarrow K(4^2S_{1/2}) + h\nu_p$		$\tau_4 = 26.37 \times 10^{-9}$s
5	$K(4^2P_{1/2}) \rightarrow K(4^2S_{1/2}) + h\nu_l$		$\tau_5 = 26.72 \times 10^{-9}$s
	Quenching		
6	$K(4^2P_{3/2})+M \rightarrow K(4^2S_{1/2})+M$	0.01 A^2 (He and CH_4)	
7	$K(4^2P_{1/2})+M \rightarrow K(4^2S_{1/2})+M$	same as 6	
	Photoexcitation		
8	$K(4^2P_{3/2,1/2}) + h\nu_{p,l} \rightarrow K(4^2D_{3/2,5/2}$ $5^2P_{3/2,1/2}$ and $6^2S_{1/2})$		Ref. 23
	Energy pooling		
9	$2K(4^2P_{3/2,1/2}) \rightarrow K(4^2D_{3/2,5/2}, 5^2P_{3/2,1/2}$ and $6^2S_{1/2}) + K(4^2S_{1/2})$		Ref. 23
	Spontaneous emission		s^{-1}
10	$K(4^2D_{5/2,3/2}) \rightarrow K(4^2P_{3/2}) + h\nu$		2.0640×10^4
12	$K(4^2D_{5/2,3/2}) \rightarrow K(4^2P_{1/2}) + h\nu$		1×10^4
13	$K(4^2D_{5/2,3/2}) \rightarrow K(5^2P_{3/2,1/2}) + h\nu$		3.428×10^6
14	$K((6^2S_{1/2}) \rightarrow K(4^2P_{3/2}) + h\nu$		3.9×10^6
15	$K(6^2S_{1/2}) \rightarrow K(4^2P_{1/2}) + h\nu$		2.72×10^6
16	$K(6^2S_{1/2}) \rightarrow K(5^2P_{3/2,1/2}) + h\nu$		4.8×10^6
17	$K((5^2P_{3/2,1/2}) \rightarrow K(4^2S_{1/2}) + h\nu$		1.13×10^6
18	$K(5^2P_{3/2,1/2}) \rightarrow K(4^2P_{3/2}) + h\nu$		4.0253×10^6
19	$K(5^2P_{3/2,1/2}) \rightarrow X(4^2P_{1/2}) + h\nu$		2.0414×10^6
	Photoionization		
20	$K(4^2D_{3/2,5/2}, 5^2P_{3/2,1/2}, 6^2S_{1/2}) + h\nu_{p,l} \rightarrow K^+ + e$		Ref. 23
	Penning ionization		
21	$K(4^2D_{3/2,5/2}, 5^2P_{3/2,1/2}, 6^2S_{1/2}) + K(4^2P_{3/2,1/2}) \rightarrow K^+ + K(4^2S_{1/2}) + e$, total 10 reactions		Ref. 23
	Recombination		
22	$K^+ + 2K \rightarrow K_2^+ + K$		2.4×10^{-33} (293.15/T) m^6/s
23	$K^+ + K + He \rightarrow K_2^+ + He$		2.4×10^{-35} (293.15/T) m^6/s
24	$K_2^+ + e \rightarrow K(4^2D_{3/2,5/2}, 5^2P_{3/2,1/2}, 6^2S_{1/2}) + K(4^2S_{1/2})$		52.6×10^{-14}, 1×10^{-14} or 0 m^3/s
25	$K^+ + e + e \rightarrow K(4^2D_{3/2,5/2}, 5^2P_{3/2,1/2}, 6^2S_{1/2}) + e$		$2.4 \times 10^{-22} \times T^{-4.2}$ m^6/s
26	$K^+ + e + M$ (He, CH4) $\rightarrow K(4^2D_{3/2,5/2}, 5^2P_{3/2,1/2}, 6^2S_{1/2}) + e$		$4 \times 10^{-41} \times (T/625)^{-2.5}$ m^6/s
	Quenching of the higher levels		
27	$K(4^2D_{5/2,3/2})+CH_4 \rightarrow K(5^2P_{3/2,1/2}) + CH_4$	25.1×10^{-20} m^2	
28	$K(6^2S_{1/2})+CH_4 \rightarrow K(6^2P_{3/2,1/2}) + CH_4$	82.6×10^{-20} m^2	
29	$K(5^2P_{3/2,1/2}) + CH_4 \rightarrow K(4^2P_{3/2,1/2})+CH_4$	37.8×10^{-20} m^2	
30	$K(4^2D_{5/2,3/2})+He \rightarrow K(5^2P_{3/2,1/2}) + He$		5.53×10^{-18}
31	$K(6^2S_{1/2})+He \rightarrow K(5^2P_{3/2,1/2}) + He$		2.32×10^{-18}
32	$K(4^2D_{5/2,3/2})+He \rightarrow K(4^2P_{3/2,1/2}) + He$		1.11×10^{-17}
33	$K(5^2P_{3/2,1/2}) + He \rightarrow K(4^2P_{3/2,1/2})+He$		1.11×10^{-18}
34	$K(6^2S_{1/2})+He \rightarrow K(4^2P_{3/2,1/2}) + He$		5.53×10^{-18}
	Electron heating and energy losses		
35	$e + K(4^2P_{3/2,1/2}) \rightleftarrows e_{hot} + K(4^2S_{1/2})$		Refs. 41 and 42
36	$e_{hot} + CH_4 \rightleftarrows e + CH_4(\nu_2, \nu_4)$.		Ref. 43
37	$e_{hot} + He \rightarrow e + He$		Refs. 44 and 45

Table 2. Kinetic processes in Rb DPAL[a]

No.	Process	Cross section	Rate constant	Ref.
	Pumping			
1	$Rb(5^2S_{1/2}) + h\nu_p \rightarrow Rb(5^2P_{3/2})$	Eq. (13) from Ref. [46]		46
	Relaxation			
2	$Rb(5^2P_{3/2})+M \rightarrow Rb(5^2P_{1/2})+M$			
	M = CH_4	42.3 Å^2		47
	M = He		$[2.34(T/300)^{3.5}+9.59(T/300)]x10^{-19}$ m^3/s	48
	Lasing			
3	$Rb(5^2P_{1/2}) + nh\nu_l \rightarrow Rb(5^2S_{1/2}) + (n+1)h\nu_l$	Eq. (20) from Ref. [46]		46
	Spontaneous emission			
4	$Rb(5^2P_{3/2}) \rightarrow Rb(5^2S_{1/2}) + h\nu_p$		τ_4 = 26.2 x10^{-9}s	49
5	$Rb(5^2P_{1/2}) \rightarrow Rb(5^2S_{1/2}) + h\nu_l$		τ_5 = 27.7 x10^{-9}s	49
	Quenching			
6	$Rb(5^2P_{3/2})+CH_4 \rightarrow Rb(5^2S_{1/2})+CH_4$	7.52e-3 Å^2		47
7	$Rb(5^2P_{1/2})+CH_4 \rightarrow Rb(5^2S_{1/2})+CH_4$	7.52e-3 Å^2		47
	Photoexcitation			
8	$Rb(5^2P_{3/2,1/2}) + h\nu_{p,l} \rightarrow Rb(5^2D_{3/2,5/2}$ $6^2P_{3/2,1/2}$ and $7^2S_{1/2})$	Eq. (13) from Ref. [50] with broadening rate of 60 MHz/torr		51,52
	Energy pooling			51, 53
9	$2Rb(5^2P_{3/2}) \rightarrow Rb(5^2D_{3/2,5/2}) + Rb(5^2S_{1/2})$	310 Å^2		
10	$2Rb(5^2P_{3/2}) \rightarrow Rb(7^2S_{1/2}) + Rb(5^2S_{1/2})$	32.1 Å^2		
11	$2Rb(5^2P_{3/2}) \rightarrow Rb(6^2P_{3/2,1/2}) + Rb(5^2S_{1/2})$	0.45 Å^2		
12	$2Rb(5^2P_{1/2}) \rightarrow Rb(5^2D_{3/2,5/2}) + Rb(5^2S_{1/2})$	78 Å^2		
13	$2Rb(5^2P_{1/2}) \rightarrow Rb(6^2P_{3/2,1/2}) + Rb(5^2S_{1/2})$	0.45 Å^2		
14	$Rb(5^2P_{1/2}) + Rb(5^2P_{3/2}) \rightarrow Rb(5^2D_{3/2,5/2}) + Rb(5^2S_{1/2})$	290 Å^2		
	Spontaneous emission		s^{-1}	54
15	$Rb(5^2D_{5/2,3/2}) \rightarrow Rb(5^2P_{3/2}) + h\nu$		1.8x10^6	
16	$Rb(5^2D_{5/2,3/2}) \rightarrow Rb(5^2P_{1/2}) + h\nu$		8.48 x10^5	
17	$Rb(5^2D_{5/2,3/2}) \rightarrow Rb(6^2P_{3/2,1/2}) + h\nu$		1.5 x10^6	
18	$Rb((7^2S_{1/2}) \rightarrow Rb(5^2P_{3/2}) + h\nu$		3.87 x10^6	
19	$Rb(7^2S_{1/2}) \rightarrow Rb(5^2P_{1/2}) + h\nu$		2.02 x10^6	
20	$Rb(7^2S_{1/2}) \rightarrow Rb(6^2P_{3/2,1/2}) + h\nu$		4.26 x10^6	
21	$Rb((6^2P_{3/2,1/2}) \rightarrow Rb(5^2S_{1/2}) + h\nu$		1.59 x10^6	
22	$Rb(6^2P_{3/2,1/2}) \rightarrow Rb(5^2P_{3/2}) + h\nu$		4.26x10^6	
23	$Rb(6^2P_{3/2,1/2}) \rightarrow Rb(5^2P_{1/2}) + h\nu$		2.2 x10^6	
	Photoionization			
24	$Rb(5^2D_{3/2,5/2}, 6^2P_{3/2,1/2}, 7^2S_{1/2}) + h\nu_{p,l} \rightarrow K^+ + e$	0.16A^2 for $5^2D_{3/2,5/2}$ 0.15A^2 for $6^2P_{3/2,1/2}$		51,53
	Penning ionization			
25	$Rb(5^2D_{3/2,5/2}, 6^2P_{3/2,1/2}, 7^2S_{1/2}) + Rb(5^2P_{3/2,1/2}) \rightarrow Rb^+ + Rb(5^2S_{1/2}) + e$, total 10 reactions		4.5x10^{-14}m^3/s for $5^2D_{3/2,5/2}$ and $6^2P_{3/2,1/2}$ 2x10^{-14}m^3/s for $7^2S_{1/2}$	51,53
	Recombination			1[b]
26	$Rb^+ + 2Rb \rightarrow Rb_2^+ + Rb$		2.4 x 10^{-33} (293.15/T) m^6/s	

27	$Rb^+ + Rb + He \rightarrow Rb_2^+ + He$		2.4×10^{-35} (293.15/T) m^6/s	
28	$Rb_2^+ + e \rightarrow Rb(5^2D_{3/2,5/2}, 6^2P_{3/2,1/2}, 7^2S_{1/2}) + Rb(5^2S_{1/2})$		1×10^{-14} m^3/s	
29	$Rb^+ + e + e \rightarrow Rb(5^2D_{3/2,5/2}, 6^2P_{3/2,1/2}, 7^2S_{1/2}) + e$		$2.4 \times 10^{-22} \times T^{-4.2}$ m^6/s	
30	$Rb^+ + e + M$ (He, CH_4) $\rightarrow Rb(5^2D_{3/2,5/2}, 6^2P_{3/2,1/2}, 7^2S_{1/2}) + e$		$4 \times 10^{-41} \times (T/625)^{-2.5}$ m^6/s	
	Quenching of the higher levels			
31	$Rb(5^2D_{5/2,3/2}) + CH_4 \rightarrow Rb(6^2P_{3/2,1/2}) + CH_4$	84 A^2		35
32	$Rb(7^2S_{1/2}) + CH_4 \rightarrow Rb(6^2P_{3/2,1/2}) + CH_4$	84 A^2		35
33	$Rb(6^2P_{3/2,1/2}) + CH_4 \rightarrow Rb(5^2P_{3/2,1/2}) + CH_4$	84 A^2 Branching ratios 2/3, 1/3		35
34	$Rb(5^2D_{5/2,3/2}) + He \rightarrow Rb(6^2P_{3/2,1/2}) + He$		2.27×10^{-18}	23[b]
35	$Rb(7^2S_{1/2}) + He \rightarrow Rb(6^2P_{3/2,1/2}) + He$		3.58×10^{-19}	23
36	$Rb(5^2D_{5/2,3/2}) + He \rightarrow Rb(5^2P_{3/2,1/2}) + He$		2.29×10^{-18}	23
37	$Rb(6^2P_{3/2,1/2}) + He \rightarrow Rb(5^2P_{3/2,1/2}) + He$		1.64×10^{-19}	23
38	$Rb(7^2S_{1/2}) + He \rightarrow Rb(5^2P_{3/2,1/2}) + He$		8.52×10^{-19}	23
	Electron heating and energy losses			
39	$e + Rb(5^2P_{3/2,1/2}) \rightleftarrows e_{hot} + Rb(5^2S_{1/2})$			1
40	$e_{hot} + CH_4 \leftrightarrow e + CH_4(\nu_2, \nu_4)$.			1
41	$e_{hot} + He \rightarrow e + He$			1

[a]For the rate constants not shown in the Table the values indicated in the relevant references were used.

[b]Rate constants of recombination and quenching of the high electronic levels by He were assumed to be the same as for K [1, 23].

VII. References (works supported by the U.S. Air Force Office of Scientific Research are marked with *)

[1] K. Waichman, B.D. Barmashenko, and S. Rosenwaks, "Dependence of static K DPAL performance on addition of methane to He buffer gas: 3D CFD modeling and comparison with experimental results," J. Opt. Soc. Am. B **36**, 3464 (2019).*

[2] K. Waichman, B.D. Barmashenko, and S. Rosenwaks, "Velocity dependence of the performance of flowing-gas K DPAL with He and He/CH_4 buffer gases: 3D CFD modeling and comparison with experimental results," J. Opt. Soc. Am. B **37**, 2209 (2020).*

[3] B.D. Barmashenko, K. Waichman, and S. Rosenwaks, "Modeling of K and Rb DPALs," Proc. SPIE 11867, 118670N (2021).*

[4] K. Waichman, B.D. Barmashenko, and S. Rosenwaks, "3D CFD modeling of flowing-gas Rb DPALs: effects of buffer gas composition and of ionization of high lying Rb states," J. Opt. Soc. Am. B 38, 3523-3531 (2021).*

[5] I. Auslender, E. Yacoby, B.D. Barmashenko and S. Rosenwaks, “Measuring and modelling the beam quality in cesium DPALs,” Proc. SPIE **11162**, 111620B (2019).*

[6] I. Auslender, E. Yacoby, B.D. Barmashenko and S. Rosenwaks, “Controlling the beam quality in DPALs by changing the resonator parameters,” Appl. Phys. B **126**, 91 (2020).*

[7] W.F. Krupke, “Diode pumped alkali lasers (DPALs) — A review (rev1),” J. Prog. Quantum Electron. 36, 4-28 (2012).

[8] B.V. Zhdanov and R.J. Knize, “Review of alkali laser research and development”, Optical Engineering 52, 0210101 (2013).

[9] G.A. Pitz and M.D. Anderson, “Recent advances in optically pumped alkali lasers”, Appl. Phys. Rev. 4, 041101 (2017).

[10] B.V. Zhdanov, M.D. Rotondaro, M.K. Shaffer and R.J. Knize, “Low-pressure cesium and potassium diode pumped alkali lasers: pros and cons,” Opt. Eng. 55, 026105 (2016).

[11] G.A. Pitz, “Characterization of a diode pumped alkali laser with a flowing gain medium,” presentation at HPLS&A 2018 Conference, Frascati, Italy, 2018.

[12] G.A. Pitz, D.M. Stalnaker, E.M. Guild, B.Q. Oliker, P. J. Moran, S.W. Townsend and D. A. Hostutler, “Advancements in flowing diode pumped alkali lasers,” Proc. SPIE 9729, 972902 (2016).

[13] B.V. Zhdanov, M.D. Rotondaro, M.K. Shaffer and R.J. Knize, “Examination of potassium diode pumped alkali laser using He, Ar, CH_4 and C_2H_6 as buffer gas,” Opt. Exp. 25, 30793 (2017).

[14] M.D. Rotondaro, B.V Zhdanov, M.K. Shaffer and R.J. Knize, “Measurement of potassium electronic-level relaxation cross-sections induced by methane,” Journal of Directed Energy 6, 182 (2017).

[15] A. J. Wallerstein, “Kinetics of higher lying potassium states after excitation of the D_2 transition in the presence of helium,” Dissertation, Air Force Institute of Technology, 2018.

[16] K. Waichman, B.D. Barmashenko, and S. Rosenwaks, "CFD DPAL modeling for various schemes of flow configurations", Proc. SPIE 9251, 92510U (2014).

[17] K. Waichman, B.D. Barmashenko, and S. Rosenwaks, "CFD assisted simulation of temperature distribution and laser power in pulsed and CW pumped static gas DPALs", Proc. SPIE 9650 96500C (2015).

[18] Y. Momozaki and M. S. El-Genk, "Dissociative recombination coefficient for low temperature equilibrium cesium plasma," J. Appl. Phys. 92, 690–697 (2002).

[19] L. P. Harris, "Ionization and Recombination in Cesium-Seeded Plasmas near Thermal Equilibrium," J. Appl. Phys. 36, 1543-1553 (1965).

[20] H**.** Wang, Z**.** Yang W**.** Hua, X**.** Xu and Q. Lu, "Choice of alkali element for DPAL scaling, a numerical study," Opt. Commun. **296**, 101-105 (2013).

[21] P.J. Wisoff, "Diode pumped alkaline laser system: A high powered, low SWaP directed energy option for ballistic missile defense high-level summary – April 2017," LLNL-TR-730237 (2017); https://www.osti.gov/servlets/purl/1357366/.

[22] A. Gavrielides, L.A. (Vern) Schlie, R. D. Loper, M.R. Hawks, and G.P. Perram, "Analytic treatment of beam quality and power efficiency in a high-power transverse flow diode pumped alkali laser," J. Opt. Soc. Am. B **35**, 2202-2210 (2018).

[23] A. J. Wallerstein, G. P. Perram and C.A. Rice, "Excitation of higher lying states in a potassium diode-pumped alkali laser," Appl. Phys. B (2019) 125:145. https://doi.org/10.1007/s00340-019-7258-0.

[24] A.I. Florescu-Mitchell and J.B.A. Mitchell, "Dissociative recombination," Physics Reports **430**, 277 – 374 (2006).

[25] H.-J. Werner, P. J. Knowles, G. Knizia, F. R. Manby, M. Schütz, P. Celani, W. Györffy, D. Kats, T. Korona, R. Lindh, A. Mitrushenkov, G. Rauhut, K. R. Shamasundar, T. B. Adler, R. D. Amos, A. Bernhardsson, A. Berning, D. L. Cooper, M. J. O. Deegan, A. J. Dobbyn, F. Eckert, E. Goll, C. Hampel, A. Hesselmann, G. Hetzer, T. Hrenar, G. Jansen, C. Köppl, Y. Liu, A. W. Lloyd, R. A. Mata, A. J. May, S. J. McNicholas, W. Meyer, M. E. Mura, A. Nicklaß, D. P. O'Neill, P. Palmieri, D. Peng, K. Pflüger, R. Pitzer, M. Reiher, T. Shiozaki, H. Stoll, A. J. Stone, R. Tarroni, T. Thorsteinsson and M. Wang, "MOLPRO, a package of ab initio programs," see http://www.molpro.net.

[26] I. Auslender, B. D. Barmashenko and S. Rosenwaks, "Multi-transverse mode operation of alkali vapor lasers: modeling and comparison with experiments," Opt. Express **25**, 19767-19779 (2017).

[27] I. Auslender, E. Yacoby, B.D. Barmashenko, and S. Rosenwaks, "General model of DPAL output power and beam quality dependence on pump beam parameters: experimental and theoretical studies", J. Opt. Soc. Am. B 35, 3134-3142 (2018).

[28] A.E. Siegman, "Output beam propagation and beam quality from a multimode stable-cavity laser", IEEE J. Quantum Electron. 29, 1212-1217 (1993).

[29] B. D. Barmashenko, and S. Rosenwaks, "Feasibility of supersonic diode pumped alkali lasers: model calculations," Appl. Phys. Lett. 102(14), 141108, 1-4 (2013).

[30] E. Yacoby, K. Waichman, O. Sadot, B. D. Barmashenko, and S. Rosenwaks, "Modeling of supersonic diode pumped alkali lasers," J. Opt. Soc. Am. B 32(9), 1824-1833 (2015).

[31] E. Yacoby, K. Waichman, O. Sadot, B.D. Barmashenko, S. Rosenwaks, "Flowing gas diode pumped alkali lasers: theoretical analysis of transonic vs. supersonic and subsonic devices," Opt. Exp. 24, 5469-5477 (2016).

[32] S. L. Guberman, "Potential Curves for the Dissociative Recombination of CO+," J.Phys. Chem. A 117, 9704-9711 (2013).

[33] Djamal Rabli, Ronald McCarroll, "The low-lying adiabatic states of the K_2^+ alkali dimer," Chem. Phys. Lett., 723, 82-88 (2019).

[34] Peter Atkins and Ronald Friedman, *Molecular Quantum Mechanics*, New York: Oxford University Press, 2011.

[35] V. N. Azyazov, S. M. Bresler, A. P. Torbin, A. M. Mebel, and M. C. Heaven," Removal of Rb(6^2P) by H_2, CH_4, and C_2H_6," Opt. Lett. 41, 669-672 (2016).

[36] I. N. Siara and L. Krause, "Inelastic Collisions between Excited Alkali Atoms and Molecules. VIII. $6^2P_{1/2}$–$6^2P_{3/2}$ Mixing and Quenching in Mixtures of Rubidium with H_2, HD, D_2, N_2, CH_4, and CD_4," Can. J.Phys. 51, 257-265 (1973).

[37] M. C. Heaven, "Potential energy surfaces for the interactions of excited Rb and Cs atoms with methane", Proc. SPIE 8238, 823808 (2012).

[38] E. Bauer. E.R. Fisher and F.R. Gilmore, "De-excitation of Electronically Excited Sodium by Nitrogen," J. Chem. Phys. **51**, 4173-4181(1969).

[39] J. R. Barker, "A modified model for quenching and electronic—vibrational energy transfer," Chem. Phys. **18**, 175-188 (1976).

[40] L. D. Landau and E. M. Lifshitz, *Quantum Mechanics, Non-Relativistic Theory.* (London-Paris 1958. Pergamon Press), pp. 322-331.

[41] A. H. Markosyan and M. J. Kushner, "Plasma formation in diode pumped alkali lasers sustained in Cs," J. Appl. Phys. **120**, 193105 (2016).

[42] O. Zatsarinny, K. Bartschat, N. Yu. Babaeva, and M. J. Kushner, "Electron collisions with cesium atoms—benchmark calculations and application to modeling an excimer-pumped alkali laser," Plasma Sources Sci. Technol. **23**, 035011 (2014).

[43] Mi-Young Song, Jung-Sik Yoon, Hyuck Cho, Yukikazu Itikawa, G. P. Karwasz, V. Kokoouline, Y. Nakamura, and J. Tennyson, "Cross Sections for Electron Collisions with Methane," J.Phys. Chem. Ref. Data **44**, 023101 (2015).

[44] Ya. B. Zeldovich and Yu. P. Raizer, *Physics of Shock Waves and High-Temperature Hydrodynamic Phenomena* (Academic, 1966).

[45] Yu. P. Raizer, *Gas Discharge Physics* (Springer, 1997).

[46] K. Waichman, B.D. Barmashenko and S. Rosenwaks, "Computational fluid dynamics modeling of subsonic flowing-gas diode pumped alkali lasers: Comparison with semi-analytical model calculations and with experimental results," J. Opt. Soc. Am. B **31**, 2628-2636 (2014).

[47] M.A. Gearba, J.H. Wells, P.H. Rich, J.M. Wesemann, L.A. Zimmerman, B.M. Patterson, R.J. Knize, and J.F. Sell, "Collisional excitation transfer and quenching in Rb(5P)-methane mixtures," Phys. Rev. A **99**, 022706 (2019).

[48] D.E. Weeks, C.D. Lewis, L.A. Schlie and G.P. Perram, "Temperature dependence of the fine structure mixing induced by ^{4}He and ^{3}He in K and Rb Diode Pumped Alkali Lasers," Appl. Phys. B **126**, 79 (2020).

[49] J. E. Sansonetti, "Wavelengths, Transition Probabilities, and Energy Levels for the Spectra of Rubidium (RbI through RbXXXVI)," J. Phys. Chem. Ref. Data **35**, 301-421 (2006).

[50] B. D. Barmashenko and S. Rosenwaks, "Detailed analysis of kinetic and fluid dynamic processes in diode-pumped alkali lasers," J. Opt. Soc. Am. B **30**, 1118–1126 (2013).

[51] A.J. Wallerstein, G. Perram and C.A. Rice, "Excitation of higher lying energy states in a rubidium DPAL," Proc. SPIE 10511, 105112J (2018).

[52] M.R. Guy, E.M. Guild, J.W. Young, I.O. Sheets, G.A. Pitz, "Pressure induced hyperfine shift and broadening rates of the $5^2S_{1/2}\rightarrow6^2P_{1/2}$ and $5^2S_{1/2}\rightarrow6^2P_{3/2}$ transitions of rubidium with He, Ar, CH_4, and C_2H_6," JQSRT **169**,14-22 (2016).

[53] X. Zhao, Z. Yang, W. Hua, H. Wang and X. Xu, "Ionization degree measurement in the gain medium of a hydrocarbon-free rubidium vapor laser operating in pulsed and CW modes," Opt. Exp. **25**, 9458-9470 (2017).

[54] O.S. Heavens, "Radiative transition probabilities of the lower excited states of the alkali metals," JOSA **51**, 1058-1061 (1961).